Accumulation mode aerosol, pockets of open cells, and particle nucleation in the remote subtropical Pacific marine boundary layer

Markus D. Petters,[1,2] Jefferson R. Snider,[1] Bjorn Stevens,[3] Gabor Vali,[1] Ian Faloona,[4] and Lynn M. Russell[5]

Received 13 December 2004; revised 22 June 2005; accepted 22 July 2005; published 25 January 2006.

[1] We analyze a marine boundary layer cloud field encountered during the second research flight of the second Dynamics and Chemistry of Marine Stratocumulus Experiment. The cloud field is distinguished by the presence of pockets of open cells. Differences between the pockets and the surrounding stratocumulus clouds are studied utilizing in situ and satellite data. The pockets are characterized as regions where cloud radar echo tops are unusually variable, accumulation mode aerosol concentrations are low, and Aitken mode particles with a mode diameter at 0.02 μm dominate aerosol number concentration. The Aitken mode particles are thought to be generated by a nucleation event which occurred within the marine boundary layer. The low accumulation mode concentrations associated with the pockets are proposed to be necessary for their maintenance.

Citation: Petters, M. D., J. R. Snider, B. Stevens, G. Vali, I. Faloona, and L. Russell (2006), Accumulation mode aerosol, pockets of open cells, and particle nucleation in the remote subtropical Pacific marine boundary layer, *J. Geophys. Res.*, *111*, D02206, doi:10.1029/2004JD005694.

1. Introduction

[2] Cloud condensation nuclei (CCN) play a critical role in the formation [*Hegg*, 1999], lifetime [*Albrecht*, 1989], and dissipation [*Ackerman et al.*, 1993] of marine stratocumulus clouds. All of these studies focus on connections between CCN, the generation of drizzle, and CCN scavenging. An important effect of drizzle is the reduction of height-integrated cloud liquid water content (LWC), commonly known as the cloud liquid water path (LWP). Where the LWP is reduced, the cloud infrared (IR) radiative cooling rate is decreased [*Stephens*, 1978; *Nicholls*, 1984] and the cloud topped marine boundary layer (MBL) may transition to a sea fog [*Ackerman et al.*, 1993]. *Stevens et al.* [1998] show in their simulation of drizzling and nondrizzling stratocumulus that drizzle stabilizes the boundary layer via its action on the budgets of heat and water substance. A plausible consequence may be the transition from stratocumulus-like to cumulus-like MBL circulation forming in response to drizzle [*Stevens et al.*, 1998]. The latter seems supported by observations of pockets of open cells which are persistent regions where open cell structure and heavy drizzle interrupt a more uniform stratocumulus cloud deck [*Stevens et al.*, 2005]. These authors focus on the remotely sensed macrophysical characteristics of pockets of open cells. Utilizing data from the same measurement platforms, we extend their analysis, placing emphasis on cloud and aerosol properties and their relationship to the macrophysical characteristics of pockets of open cells.

[3] Effects of CCN on cloud droplet number concentration (CDNC), cloud droplet effective radius (r_e), and albedo are well documented [*Houghton et al.*, 2001, and references therein]. Equally well studied are aerosol source processes over the open oceans. These are formation via homogeneous nucleation of supersaturated vapor [*Charlson et al.*, 1987; *O'Dowd et al.*, 2002], henceforth particle nucleation, particle injection via the bubble burst process [*Blanchard and Woodcock*, 1980; *O'Dowd and Smith*, 1993; *Nilsson et al.*, 2001], and transport. Particle nucleation events have been documented in the tropical MBL [*Clarke et al.*, 1998b], close to shore [*Covert et al.*, 1992; *Hoppel et al.*, 1994; *O'Dowd et al.*, 2002], and at polar latitudes [*O'Dowd et al.*, 1997]. From these observations, as well as modeling studies of particle nucleation, it is recognized that particle nucleation rates are sensitive to the abundance of sea salt aerosol. The latter provide particle surface area onto which vapors may condense, thus relegating particle nucleation to low wind (i.e., low sea salt) regimes [e.g., *Pirjola et al.*, 2000]. Nevertheless, the case for particle nucleation in the remote MBL remains contentious, most notably because particles may also enter the MBL via transport from the free troposphere (FT) [*Covert et al.*, 1996; *Clarke et al.*, 1998b; *Russell et al.*, 1998]. Overall, the relative contributions of transport, either vertically or horizontally, versus particle nucleation and the bubble burst processes remain unclear [*Raes et al.*, 1997].

[1]Department of Atmospheric Science, University of Wyoming, Laramie, Wyoming, USA.
[2]Now at Department of Atmospheric Science, Colorado State University, Fort Collins, Colorado, USA.
[3]Department of Atmospheric Science, University of California, Los Angeles, California, USA.
[4]Department of Land, Air and Water Resources, University of California, Davis, California, USA.
[5]Scripps Institution of Oceanography, University of California, San Diego, California, USA.

0148-0227/06/2004JD005694$09.00

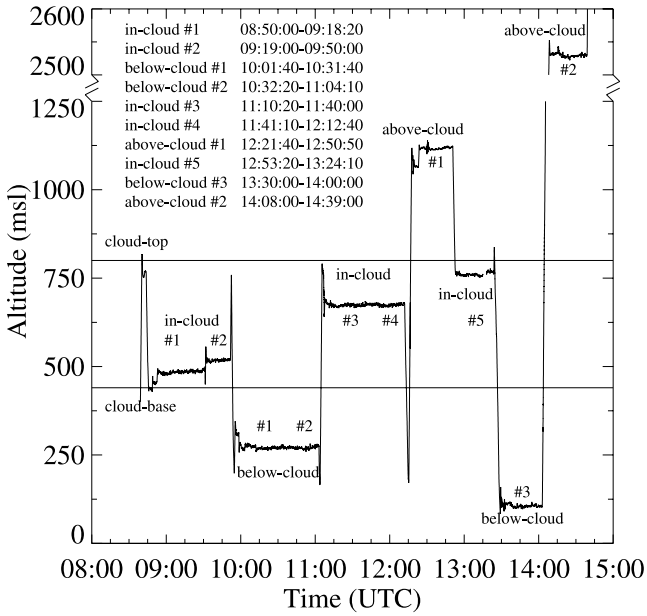

Figure 1. Height-time of the research portion of flight 2. This pattern was typical for the DYCOMS-II entrainment flights. Numbers indicate the label of the circle referred to in the text. Average cloud top and cloud base altitudes are also shown. Note the break in scale for the second above-cloud segment, flown at 2500 msl. The abbreviation "msl" denotes meters above sea level.

[4] In this study, we analyze satellite and in situ data from the second flight (flight 2, 11 July 2001) of the second Dynamics and Chemistry of Marine Stratocumulus (DYCOMS-II) experiment as a case study. In a companion study, *van Zanten and Stevens* [2005] examined the structure of drizzle within the pockets. Our emphasis is on linkages between the pockets, low accumulation mode aerosol concentration (mode diameter ~0.2 μm), and Aitken mode aerosol (mode diameter ~0.02 μm). We also present evidence that the latter likely originated via particle nucleation within the MBL. We propose mechanisms involving low accumulation mode concentrations as an important factor in the maintenance of pockets of open cells.

2. Instrumentation and Methods

2.1. DYCOMS-II

[5] The DYCOMS-II field campaign [*Stevens et al.*, 2003a] took place in July 2001, and focused on the characterization of the nocturnal cloudy MBL at a distance of ~350 km west of the southern California coastline (~32°N, 122°W). Prior studies of this stratocumulus regime were made during daytime [*Albrecht et al.*, 1988; *Lenschow et al.*, 1988]. The DYCOMS-II field program utilized the NSF/NCAR C-130 aircraft operated by the National Science Foundation and the National Center for Atmospheric Research, Boulder, CO. Seven flights employed a stepped circular flight pattern conducted both in the MBL and FT; flight 2 (11 July 2001) is the focus of this analysis. Figure 1 shows that the flight was divided into constant altitude segments of duration of 30 or 60 min. The pattern consisted of groups of one (30 min) or two (60 min) 60 km diameter circles flown above cloud, in cloud, and below cloud. Numbers indicate the label of the circle referred to in the text, e.g., in-cloud #1. Circles were flown in the clockwise direction and then in the counterclockwise direction. Ferry time to the study domain was ~35 min and the research portion of the flights (~6 hours) was a quasi-Lagrangian study focused on the MBL. This was achieved by allowing the aircraft to drift with the mean wind. During flight 2, the observed circle centerpoints lagged with respect to wind-advected positions.

[6] Average cloud depth during flight 2 was 360 m and was typical for the clouds observed during the project [*Stevens et al.*, 2003a]. Marine boundary layer CCN concentrations active at 0.44% water supersaturation were the lowest observed during the campaign (81 ± 28 cm^{-3} [*Petters*, 2004]). The circle-averaged drizzle flux at cloud base was unusually large (1.2 mm d^{-1} [*van Zanten et al.*, 2005]) and drizzle fluxes were strongest inside the pockets of open cells [*Stevens et al.*, 2005].

2.2. Instrumentation

[7] The C-130 was fitted with the aerosol and cloud microphysics probes summarized in Table 1. We refer to these instruments via the abbreviations given in parentheses adjacent to the formal probe names. The first three table entries (CCN, CN and RDMA) are aerosol instruments operated inside the fuselage of the C-130. The CN instrument [*Twohy*, 1991] sampled from a reverse-facing inlet and the CCN and RDMA sampled via a solid diffuser inlet. The last four entries of Table 1 refer to cloud microphysics probes mounted external to the fuselage, below the wings. We also utilize LWC and r_e from a PVM-100 cloud water probe [*Gerber et al.*, 1994], vertical velocity (w) from a gust probe system, downwelling IR irradiance ($F_{IR\downarrow}$) from a pyrgeometer, upwelling IR radiance expressed as radiative temperature ($T_{\uparrow}$) from a radiometer, reflectivity data from the Wyoming Cloud Radar [*Pazmany et al.*, 1994; *Vali et al.*, 1998], and satellite measured upwelling IR radiance at 11 μm expressed as brightness temperature (T_{b11}). Additional information on instrumentation and data processing are given in Appendix A and a complete description of these instruments is presented by *Stevens et al.* [2003b]. Symbols and acronyms are defined in the notation section.

2.3. Azimuthal Grid

[8] Typically, in situ data obtained from research aircraft are presented as time series. Because of the quasi-Lagrangian circular flight pattern employed during DYCOMS-II, an angular coordinate is more natural to use and allows spatial variability to be clearly seen. For this reason, we present the C-130 data versus azimuthal angle (Φ) with $\Phi = 0°$ indicating the most northern point on the C-130 circle. Larger values of Φ progress clockwise from that reference point. With the exception of C-130 data from the below-cloud #3 circle and the in-cloud #5 circle, where we plot 1 Hz data, the in situ data are shown as one degree (~5 s) averages.

2.4. Aerosol and CCN

[9] In the measurement community, CCN are defined as particles that activate to form cloud droplets when subjected to a fixed, or systematically varying, water supersaturation

Table 1. Aerosol and Cloud Microphysics Instrumentation Operated on the C-130 Aircraft During DYCOMS-II[a]

Instrument	Measurement	Size Range, μm	Channels
UWyo CCN (CCN)	CCN	$0.10\% < s^{b} < 0.99\%$	N/A
TSI 3760 CPC[c] (CN[d])	CN	$D > 0.016$	N/A
RDMA[e]	aerosol size	$0.01 < D < 0.13$	62
DMT SSP-200 (PCASP[f], AMC[g])	aerosol size	$0.1 < D < 3.0$	29
DMT SSP-100 (CDNC[h])	cloud droplets	$1 < D < 47$	40
DMT SPP-2D-25 (2D-C)	drizzle drops	$17 < D < 1592$	62
Gerber PVM-100 (LWC[i])	LWC	$3 < D < 47$	N/A

[a]Sizes are given in diameter. N/A denotes not applicable.
[b]Supersaturation.
[c]Condensation particle counter.
[d]Condensation nuclei.
[e]Radial differential mobility analyzer.
[f]Passive cavity aerosol spectrometer probe.
[g]Accumulation mode concentration.
[h]Cloud droplet number concentration.
[i]Liquid water content.

within a droplet growth chamber. Since values of the cloud droplet number concentration predicted from CCN agree with droplet concentrations measured in adiabatic regions of marine stratocumulus [*Yum et al.*, 1998; *Snider and Brenguier*, 2000] the utility of this CCN definition, as well as CCN measurement, is obvious. Conversely, the prediction of CCN from measured aerosol size spectra, which is a standard technique in the cloud modeling community, is complicated by our limited understanding of the chemical composition and mixing state of the aerosol [*Covert et al.*, 1998; *Chuang et al.*, 2000; *Zhou et al.*, 2001; *Cantrell et al.*, 2001; *Snider et al.*, 2003]. In spite of the discrepancies discussed in these references we will utilize particle concentrations, measured by the PCASP, as a surrogate for 1 Hz CCN measurements. Further we will equate the PCASP-measured concentration with the accumulation mode concentration and refer to the latter as AMC. This is not strictly correct, since the accumulation modes observed during DYCOMS-II often peaked near the minimum size detected by the PCASP (0.1 μm, Table 1). Furthermore, the PCASP also detects particles in a coarse mode centered at $D \sim 1$ μm but these do not contribute substantially to the number count reported by the PCASP. This particular application of the PCASP data set is motivated by our need for cloud droplet nuclei concentration measurements at a rate substantially larger than that provided by the UWyo CCN instrument (0.03 Hz).

2.5. Definition of the Disturbed, the Cloud-Free and the Stratiform Regions

[10] Figure 2 shows the spatial distribution of brightness temperature at 11 μm (T_{b11}) at 0900 UTC. A region of broken cloudiness is apparent to the northwest of the C-130 flight track and is delineated by the left open polygon. Apparent in the latter are pockets where open cell structures interrupt the more uniform stratocumulus cloud deck. We refer to this as the "disturbed region." An analysis of the tilde-shaped structure, henceforth "the pocket," lying along the northern border of the disturbed region is given by *Stevens et al.* [2005]. These authors demonstrate that it is composed of open cells which have an erect honeycomb structure composed of cloudy and precipitating "cell walls," surrounding an inner "cell core," where depleted amounts of condensed water (i.e., droplets and drizzle) were observed.

[11] The region to the east of the C-130 flight track, also delineated with the right-hand open polygon and with maximum T_{b11} centered at 32°N, 121°W, shows enhanced values of T_{b11} indicating reduced LWP corresponding to either very thin cloud or clear sky. We will refer to this region as the "cloud-free region." At first glance, the cloud-free region appears similar to the disturbed region. However, the temporal evolution of the disturbed and cloud-free regions is very different. Figure 3 shows the advected positions of the two open polygons marking the disturbed

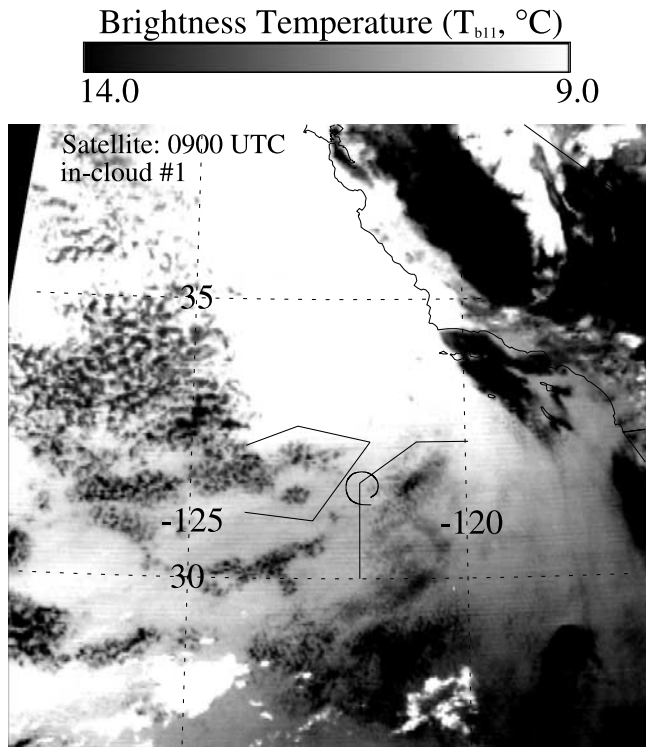

Figure 2. Spatial distribution of T_{b11} at the start of the research portion of flight 2. Time in the image indicates the time of the satellite data acquisition. The flight track of the 60 km circle most coincident with the satellite image is also depicted (cf. Figure 1). Open polygons delineate the disturbed and the stratiform region. See text for details.

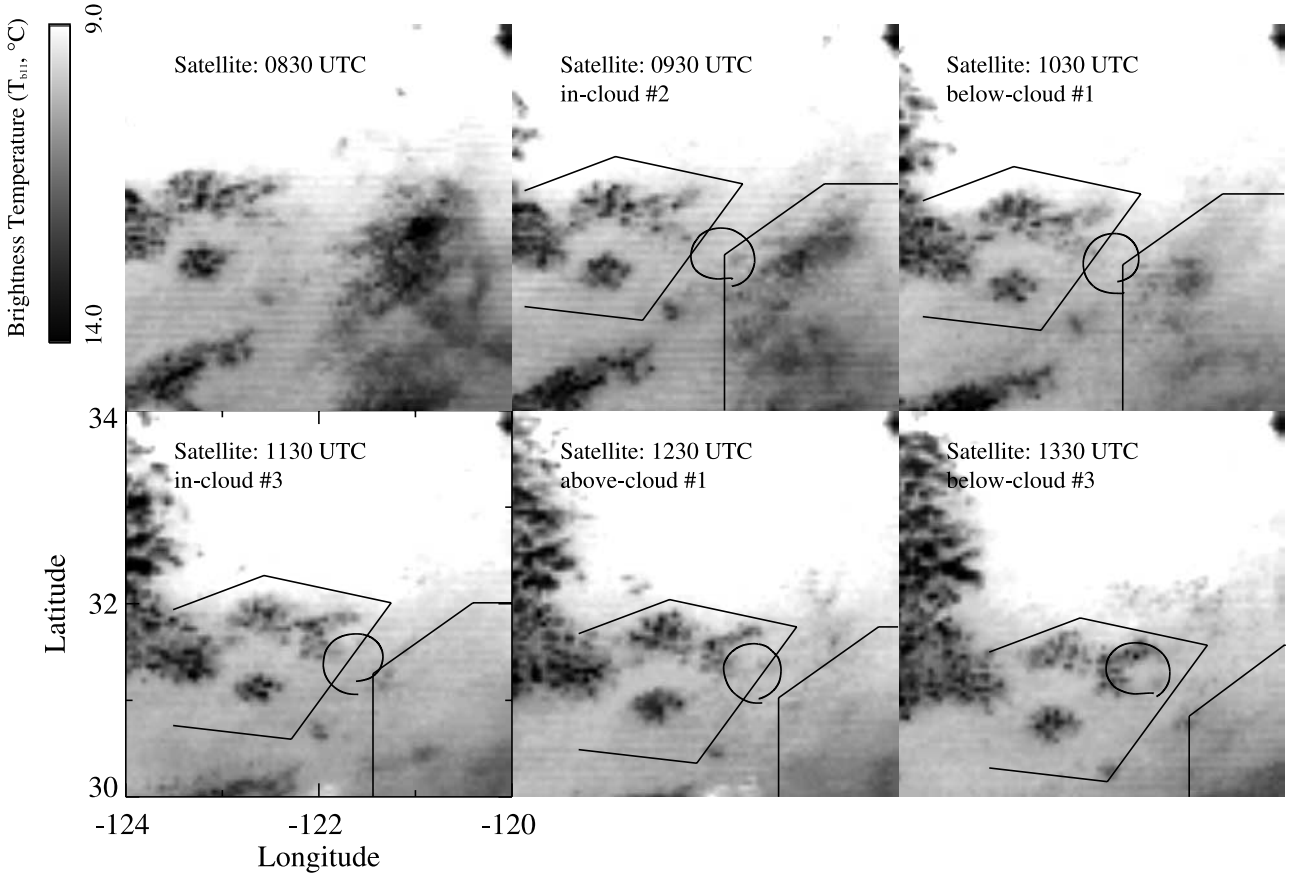

Figure 3. Temporal evolution of T_{b11} during flight 2. Satellite images are presented as in Figure 2 but with the geographic domain reduced. The open polygons delineate the disturbed and the stratiform region and are advected with the mean MBL wind. See text for details.

and the cloud-free region. These boundaries are adjusted every 30 min in accord with the wind speed and direction measured by the C-130 within the MBL. The flight track of the C-130 circle most coincident with the satellite image is also depicted. It is evident that the disturbed region is advecting into the C-130 study domain from the northwest. Furthermore, the time sequence shows that the thin clouds within the cloud-free region thickened to form a stratiform cloud layer. This thickening was completed at ~1100 UTC and subsequent to that we refer to the region enclosed by the right-hand polygon as the "stratiform region." Conversely, the disturbed region is persistent and shows little change in appearance throughout the night. No such assertion can be made about the persistence of individual cells composing the disturbed region because the spatial dimension of the cells approaches the resolution of the satellite data (4 × 4 km, Appendix A5). Between 0830 and 1430 UTC the C-130 probed both the disturbed and the stratiform region below cloud, in cloud, and above cloud. Utilizing this data we analyze and discuss aerosol, cloud, and thermodynamic properties of the two regions.

3. Results

3.1. Radar Data

[12] Contrasts between the disturbed and the stratiform regions are evident in the radar reflectivity profile data shown in Figure 4. Because of ambiguity arising from the fact that radar reflectivity varies with the 6th moment of the drop size spectrum, echoes are best interpreted as either hydrometeors suspended in the updraft (cloud), or hydrometeors with substantial velocities relative to the updraft (drizzle), or precipitation below cloud base.

[13] In the northwest quadrant of the circle, strong echoes reaching the surface are evident and interrupted by a pronounced cell core where weaker echoes do not reach the surface, and where echo tops are lower. No drizzle, and more horizontally uniform radar echoes, are evident in the stratiform region to the southeast.

3.2. Disturbed Versus Stratiform Region

[14] In Figure 5 we juxtapose C-130 data from the below-cloud #1 (bottom five left-hand plots), in-cloud #3 (middle four left-hand plots), and above-cloud #1 (top four left-hand plots) circles with satellite-retrieved values of T_{b11} (three right-hand plots). The latter show T_{b11} fields similar to Figure 3 but here the geographic domain is reduced by 50%. Results are stacked according to flight level. To first approximation we assume that data acquired during different circles, and acquired at the same Φ, are vertically aligned. This is not strictly correct, because the centers of the C-130 circles lagged behind the advected air mass (section 2.1). For this reason, we cannot resolve the vertical structure of features at scales finer than $\Delta\Phi \sim 30^\circ$ (~16 km).

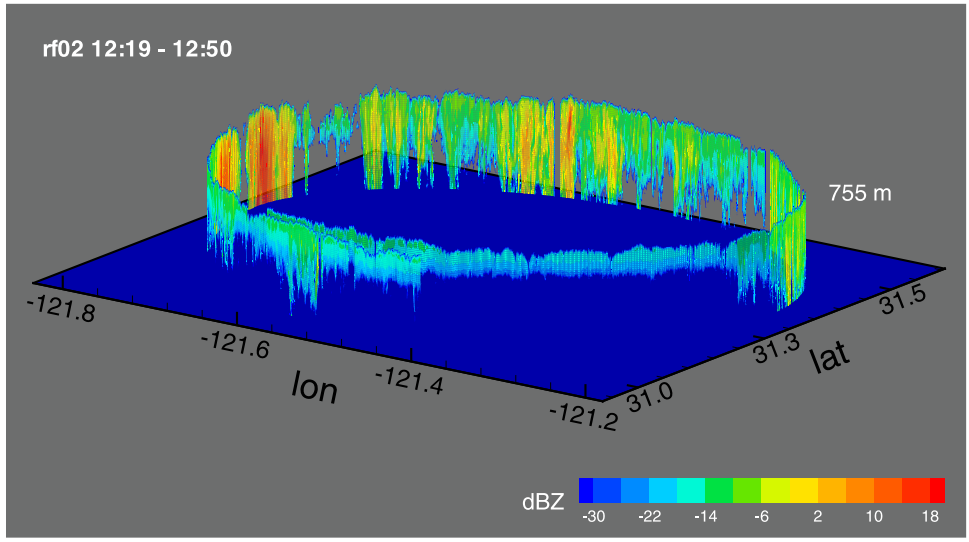

Figure 4. Three-dimensional projection of height-versus-time radar reflectivity data observed during the above-cloud #1 circle.

3.2.1. Below Cloud

[15] During the below-cloud #1 circle, potential temperature (θ) is higher and water vapor mixing ratio (r) is slightly smaller in the stratiform region. These differences translate into a contrast of lifted condensation level (LCL) between the disturbed and the stratiform region. In the disturbed region, and during the few times aerosol data are not corrupted by liquid water shattering (Appendix A), condensation nuclei concentrations are enhanced and accumulation mode concentrations are reduced compared to that in the stratiform region. A size-discriminated view of these microphysical contrasts is presented in Figure 6. Figure 6 (top) shows condensation nuclei and accumulation mode concentrations (AMC, section 2.4) observed during the below-cloud #2 circle. Vertical solid and dashed lines indicate the start and end of the RDMA scan. Drizzle did not affect either size spectrum. In the disturbed region CN-to-AMC ratios are large compared to the stratiform region and Aitken mode particles with $D \sim 0.02$ μm dominate aerosol number (Figure 6, bottom, left plot). Appreciable concentrations of Aitken mode particles are not evident in the stratiform region (Figure 6, bottom, right plot).

3.2.2. In Cloud

[16] During the in-cloud #3 circle (Figure 5), the disturbed region is distinguished by reduced cloud droplet number concentrations, larger values of r_e, and substantial concentrations of particles detected by the 2D-C probe, a surrogate for drizzle. A positive correlation of accumulation mode concentration below cloud and cloud droplet number concentration measured at similar azimuth angle is also evident. No such correlation is observed between below-cloud CN and cloud droplet number concentration. Aerosol and cloud microphysical contrasts between the disturbed region and the stratiform region are consistent with the second indirect effect of aerosols on clouds (i.e., fewer cloud droplets and larger r_e coinciding with drizzle).

3.2.3. Above Cloud

[17] The four top left plots of Figure 5 contrast air properties sampled above the disturbed and the stratiform region. In the latter, the air is warmer and dryer, $T_\uparrow$ (Appendix A5) is relatively steady, and radar echo top heights are relatively uniform. The uniform radar echo top heights in the stratiform region are in contrast with that retrieved from the disturbed region ($\Phi \sim 300°$), where reduced cloud top heights are evident in the radar echo top and $T_\uparrow$ time series. There is also evidence of locally elevated echo tops in the disturbed region, compared to average values in the stratiform region.

3.3. Internal Structure

[18] Figure 3 shows that by ~1300 UTC the C-130 track was contained within the open polygon defining the disturbed region. For times greater than 1300 UTC, i.e., during the in-cloud #5 and the below-cloud #3 circles, the C-130 acquired samples of what we have designated as "the pocket" (section 2.5) and the horizontally more stratiform cloud within the disturbed region. Figure 7 shows a sketch of C-130 sampling during the below-cloud #3 segment. In this section we emphasize data collected over all values of Φ and these are used to develop contrasts between inside and outside the pocket.

3.3.1. Below Cloud

[19] In the AVHRR satellite image in the bottom right plot of Figure 8, cell walls and cell cores are evident inside the pocket. During this circle (four bottom left plots) the C-130 sampled below cloud, and cell cores are detected by decreased $F_{IR\downarrow}$. Throughout the pocket, here defined by $10° < \Phi < 90°$ and $200° < \Phi < 300°$, there are reduced accumulation mode concentrations and enhanced CN concentrations. The relationship between the below-cloud #3 accumulation mode concentrations and $F_{IR\downarrow}$ data seen in Figure 8 is made apparent in Figure 9. Red points are acquired inside the pocket and blue points correspond to data from the surrounding stratiform cloud. Figure 9 makes the point that MBL regions associated with little or no overhead cloudiness (the cell cores) are also associated with low accumulation mode concentrations. It also excites interest in connections between droplet nuclei abundance and cloud top heights, perhaps along the lines of *Hegg* [1999].

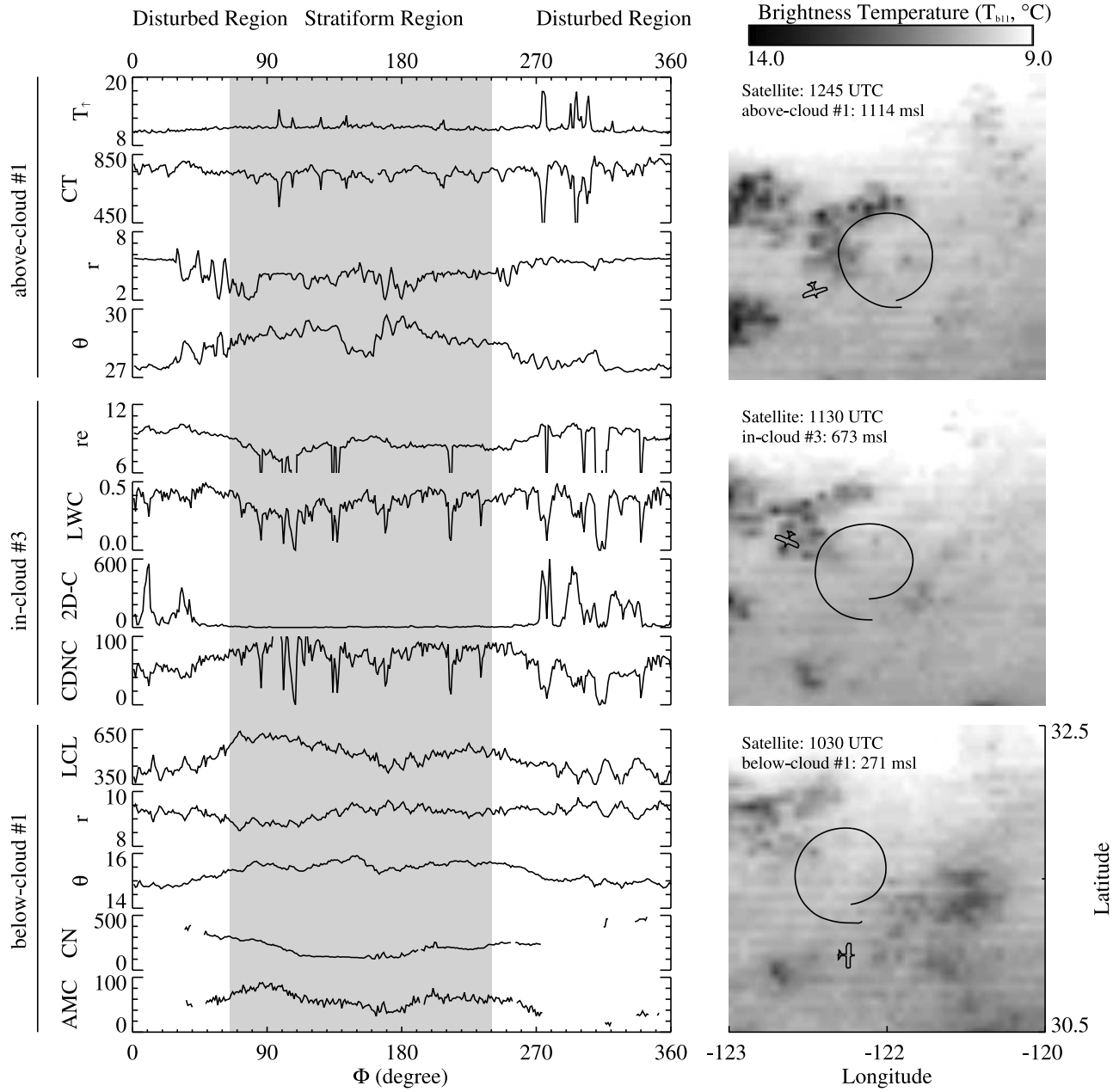

Figure 5. C-130 data corresponding to the disturbed and stratiform regions observed during the below-cloud (bottom five left-hand plots), in-cloud #3 circle (middle four left-hand plots), and above-cloud #1 circle (top four left-hand plots). Satellite images are presented as in Figure 3 but with the geographic domain reduced. The aircraft indicates the position of the C-130 at the time of the satellite image. Units are AMC (cm^{-3}), CN (cm^{-3}), θ (°C), r (g kg^{-1}), LCL (m), CDNC (cm^{-3}), 2D-C (L^{-1}), LWC (g m^{-3}), r_e (μm), CT (radar echo top height, m), and $T_\uparrow$ (°C). The shaded region delineates the extent of the stratiform region. Flight circles are "stacked" according to flight level.

[20] In Figure 10 we contrast the power spectral density ($S_w(f)$) of the below-cloud #3 w time series inside (1338–1343 UTC; 250° < Φ < 300°; dotted line) and outside the pocket (1343–1348 UTC; 300° < Φ < 360°; solid line). These times were chosen because contiguous regions are necessary to calculate $S_w(f)$ and because equal sample size ensures comparable statistical significance. We employ a method of calculating and presenting $S_w(f)$ which is area preserving (Appendix A2). Values of length scales, shown on the top abscissa, are obtained from f and the C-130 speed (108 m s^{-1}), assuming stationary isotropic turbulence. If it is also assumed that the eddies are spatially and temporally coherent, i.e., they do not dissipate within one eddy turnover time, then the peak at $f \sim 0.2$ Hz indicates that eddies of aspect ratio one dominate the turbulence field, particularly outside the pocket (solid line). Larger-scale eddies also contribute to the turbulence, evident in the peaks at lower frequency. Inside the pocket, the total w variance is reduced; that is, the area under the dotted curve is smaller relative to that outside the pocket, and this reduction in most pro-

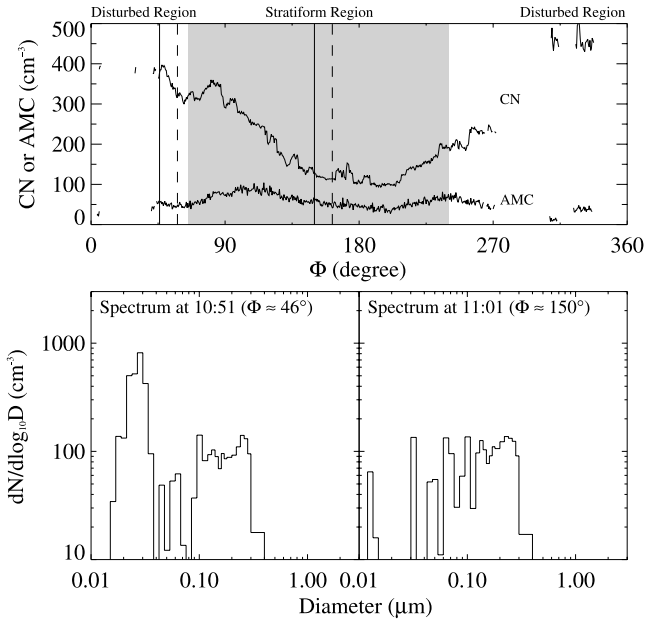

Figure 6. (top) Condensation nuclei and accumulation mode concentration (AMC) for the below-cloud #2 circle (Figure 1). (bottom) Two aerosol size spectra acquired at $\Phi \sim 46°$ and $\Phi \sim 150°$. The vertical solid and dashed lines indicate the start and end of the RDMA scan (Appendix A1). Points where cloud water or drizzle were present are removed from the time series. The shading (Figure 6, top) indicates the stratiform region (section 2.5).

nounced at $f \sim 0.2$ Hz. At lower frequencies ($f \sim 0.05$), a shift in length scales between inside and outside the pocket is also apparent. Such a shift could be indicative of turbulence that is organized at larger scales inside the pocket but may also be the result of sampling a gravity wave at two different angles, inside and outside the pocket.

[21] Vertical velocity statistics sampled inside and outside the pocket are presented in Figures 11a and 11b. Time segments corresponding to inside and outside the pocket are chosen as in Figure 10. For both time segments the w distributions (top plots) and $F_{IR\downarrow}$ distributions (bottom left plots) are shown, and these are referred to as the marginal distributions. Also presented are conditional w distributions sampled within $\Delta F_{IR\downarrow} = 10$ W m^{-2} intervals (bottom right plots). Comparing the statistics of the marginal w distributions confirms the assertion that inside the pocket the w variance is reduced, consistent with Figure 10, and also shows that the marginal w distribution is positively skewed inside the pocket. No significant trend emerges when comparing the conditionally sampled distributions inside the pocket. This comparison indicates that the turbulence fields in the cell cores, i.e., where $F_{IR\downarrow}$ is reduced, are comparable to those in the cell walls.

3.3.2. In Cloud

[22] During the in-cloud #5 circle (Figure 8, four middle left plots), the cell cores are detected by increased $T_\uparrow$. Here we employ θ as tracer of FT air and utilize cloud droplet number concentration to determine whether or not it is cloudy. An increase in θ at $30° < \Phi < 110°$ is evident. These increases are thought to be due to the presence of FT air at flight altitude as it appears from both the θ and cloud droplet number concentration time series the aircraft was sampling above the capping inversion. This is in contrast to inside the pocket, here defined by $260° < \Phi < 360°$, where θ is steady at 17°C and indicating that these in situ samples were taken within the MBL.

[23] The six top left plots of Figure 8 are an inset of the in-cloud #5 data taken inside the pocket. A correlation is apparent between the $T_\uparrow$ (indicating cell cores) and the radar reflectivity profile data. Some cores are characterized by radar reflectivities below flight level. At flight level, these particular cell cores are cloud-free (CDNC = 0 cm^{-3}), relative humidity (*RH*) is high (∼95%), and accumulation mode concentration is generally less than 40 cm^{-3}. In two cell cores (1303:40–1304:00 and 1305:50–1306:10 UTC) accumulation mode concentration is <2 cm^{-3}. The low accumulation mode concentration within the cell cores (2–40 cm^{-3}) are in marked contrast to the attendant values of CN (∼400 cm^{-3}). The latter observation is consistent with Aitken mode particles evident in the aerosol size spectrum sampled in one of the cell cores (1301:22–1302:22 UTC, Figure 8, top right plot), and also present below cloud in the disturbed region (Figure 6). The fact that aerosol microphysical properties (spectra and CN-to-AMC ratios) within the upper reaches of the MBL agree with those below cloud, strongly suggests that aerosol within the MBL is well mixed. The values of θ between 15 and 17°C both below cloud (Figure 5) and immediately below the MBL capping inversion (Figure 8), plus the observation of RH ∼95% support this assertion. In the adjacent cell walls, droplet concentrations are limited at 60 cm^{-3} and radar reflectivities extend from above flight level to the sea surface.

3.4. Summary of Cell Structure

[24] To summarize our results we present a magnified view of the structure of the open cell observed between 1300:28 and 1303:28 UTC. In Figure 12 we illustrate the LCL, flight level and estimated inversion heights, delineate between cell wall and cell core and superimpose these with the reflectivity profiles and the cloud droplet number concentration and the accumulation mode concentration time series. From the observations shown here, and those

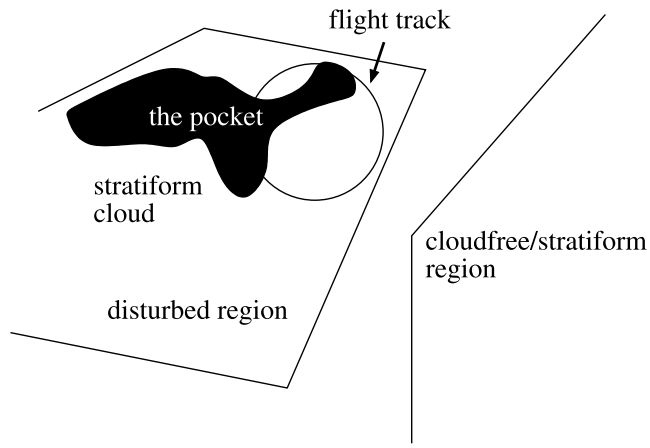

Figure 7. Sketch of the C-130 sampling the pocket and the horizontally more stratiform cloud during the below-cloud #3 circle.

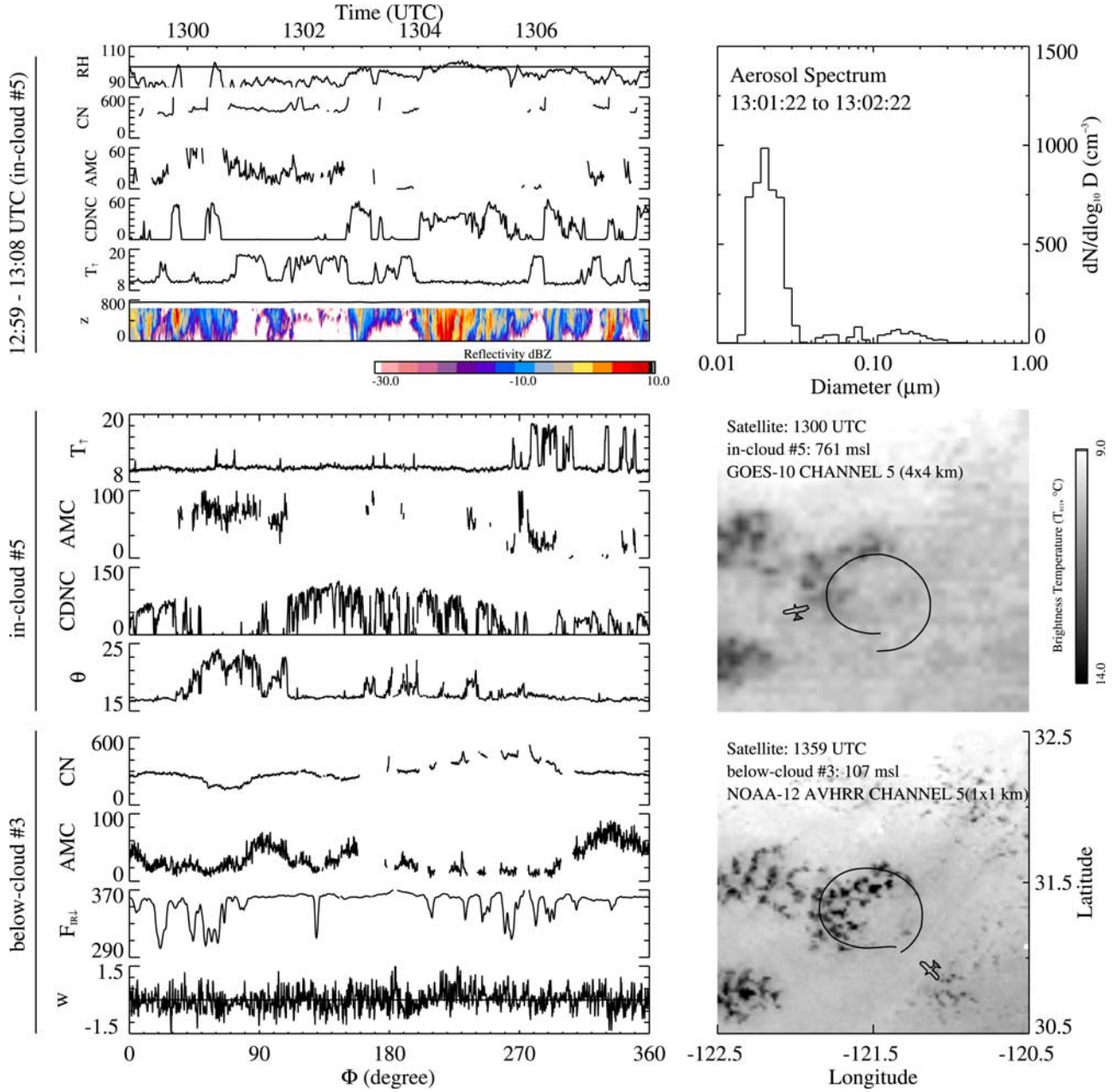

Figure 8. C-130 data corresponding to the below-cloud #3 circle (bottom four left-hand plots), in-cloud (middle four left-hand plots), and the northwest quadrant of the in-cloud #5 circle (top six left-hand plots). The right-hand plots show T_{b11} (°C) from the NOAA 12 AVHRR (bottom right plot), T_{b11} from the GOES 10 satellite (middle right plot), and the particle aerosol size spectrum (top right plot). Acquisition time interval of the aerosol size spectrum is also shown. Satellite images are presented as in Figure 5 but with the geographic domain reduced. The units are w (m s^{-1}), $F_{IR\downarrow}$ (W m^{-2}), AMC (cm^{-3}), CN (cm^{-3}), θ (°C), CDNC (cm^{-3}), $T_\uparrow$ (°C), z (msl), and RH (%). The six top left plots are an inset of the in-cloud data ($260° < \Phi < 360°$) with the corresponding times (UTC) indicated at the top. The image in the lowest of these plots is a radar reflectivity profile (dBZ), and the horizontal line indicates the C-130 flight level. The white color corresponds to data below the instrument noise threshold.

obtained from the foregoing analysis, we characterize the structure of a cell as follows: (1) Horizontally, a cell is composed of a narrow cell wall with strong radar reflectivity, and a broad cell core containing intermittent cloud or drizzle characterized by reflectivities smaller than that in the cell walls. (2) Below the LCL, radar reflectivities are more intense in the cell walls. (3) Below the LCL, and in the cell cores, the accumulation mode concentrations are limited at 40 cm^{-3} and turbulence intensity is similar to that in the cell walls. (4) The radar echo tops are higher in the cell walls and variable radar echo tops are observed in the cell core. One example of echo top height variability is apparent in the region of enhanced radar reflectivity centered at 1301:45 UTC extending with relatively low reflectivities

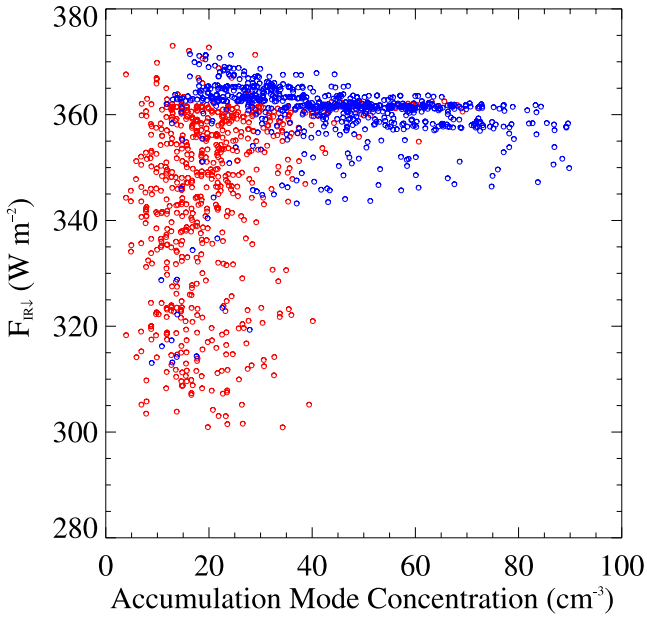

Figure 9. Scatterplot of accumulation mode concentration and $F_{IR\downarrow}$ for the below-cloud #3 circle. Data acquired inside the pocket ($10° < \Phi < 90°$ and $200° < \Phi < 300°$) are red, and data acquired elsewhere are blue.

(< −10 dBZ) to the sea surface but with radar echo tops not extending to flight level.

4. Aitken Mode Particles

[25] Here we discuss whether the Aitken particles are, or are not, effective droplet nuclei. The generally accepted theory holds that particle nucleation in the remote oceanic MBL is the result of condensing H_2SO_4 and methane sulfonic acid. These compounds are derived from photo-oxidation of dimethylsulfide vented by the ocean surface waters. Data show that in remote marine atmospheres NH_4^+ to non-sea-salt SO_4^{2-} molar ratios are often near unity [*Quinn et al.*, 1990] and thus we assume that the Aitken mode particles are composed of NH_4HSO_4.

[26] During flight 2, the maximum applied supersaturation in the UWyo CCN instrument was 1%. CCN concentrations at $s = 1\%$ did not significantly exceed those at $s < 1\%$, indicating that the Aitken particles did not activate inside the CCN instrument and demonstrates that Aitken particle activation in the cloud is contingent on $s > 1\%$. According to Köhler theory [*Snider et al.*, 2003], the critical supersaturation, i.e., the supersaturation necessary to activate a pure NH_4HSO_4 particle with $D = 0.020$ μm is 1.8%.

[27] A closed adiabatic parcel model was utilized to predict cloud droplet concentration with inputs consisting of aerosol size spectra, aerosol chemical composition, and updraft [*Snider et al.*, 2003]. Frequency distributions of cloud droplet number concentration are calculated from predictions based on an ensemble of w acquired during the below-cloud #3 circle ($250° < \Phi < 300°$, 1338–1343 UTC, Figure 11) and compared to the corresponding observed frequency distribution of cloud droplet number concentration, within the pocket ($260° < \Phi < 360°$, 1259–1308 UTC). The aerosol size spectrum inside the pocket is modeled utilizing a two mode lognormal distribution: n_1 (Aitken mode) = 404 cm^{-3}, $\bar{D}_1 = 0.020$ μm, $\sigma_1 = 1.24$; n_2 (accumulation mode) = 32 cm^{-3}, $\bar{D}_2 = 0.128$ μm, $\sigma_2 = 1.79$. These coefficients were obtained by fitting the aerosol size spectrum acquired inside a cell core (1301:22 UTC, Figure 6, top right plot). Subsequent to the fitting, the concentration of the Aitken mode (i.e., n_1) was scaled to force agreement between the total particle concentration used to initialize the parcel model and the measured CN concentration (Appendix A1). The parcel model was initialized with $T = 12°C$, $p = 945$ hPa, RH = 98%, soluble solute mass fraction of unity, and the condensation coefficient (α) either 0.04 or unity [*Pruppacher and Klett*, 1997]. Parcel model descriptions like this typically overestimate droplet concentrations which is attributed to our limited understanding of the chemical composition and mixing state of the aerosol [e.g., *Snider et al.*, 2003]. However, entrainment and collision/coalescence may reduce droplet concentration, relative to that produced by activation alone, and thus contributes to the overestimation of the predicted (adiabatic) droplet concentration [*Pawlowska and Brenguier*, 2000].

[28] Statistics presented in Figure 13 indicate that there is reasonable consistency between the predicted and observed cloud droplet ensembles, regardless of what is assumed for the condensation coefficient. The model calculations indicate that ~40 cm^{-3} should activate into cloud droplets. Of these 40 cm^{-3}, 32 cm^{-3} are drawn from the accumulation mode. Only 8 out of 404 (~2%) of the Aitken mode particles were activated by the model, because the relatively weak updrafts limit the peak supersaturation in ascending parcels. On the basis of this we assert that NH_4HSO_4 is a consistent chemical composition for the aerosol particles,

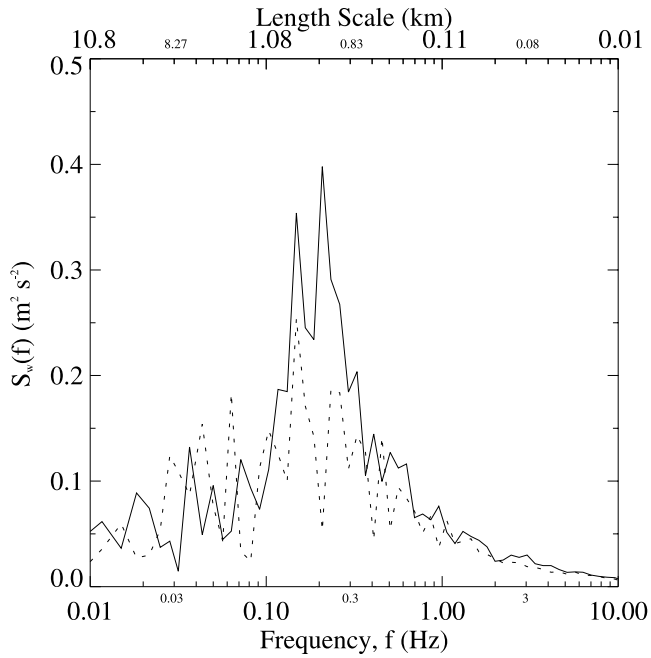

Figure 10. Power spectral density $S_w(f)$ per decimal logarithmic frequency interval obtained from the 25 Hz w time series inside (1338–1343 UTC, dotted) and outside (1343–1348 UTC, solid) the pocket.

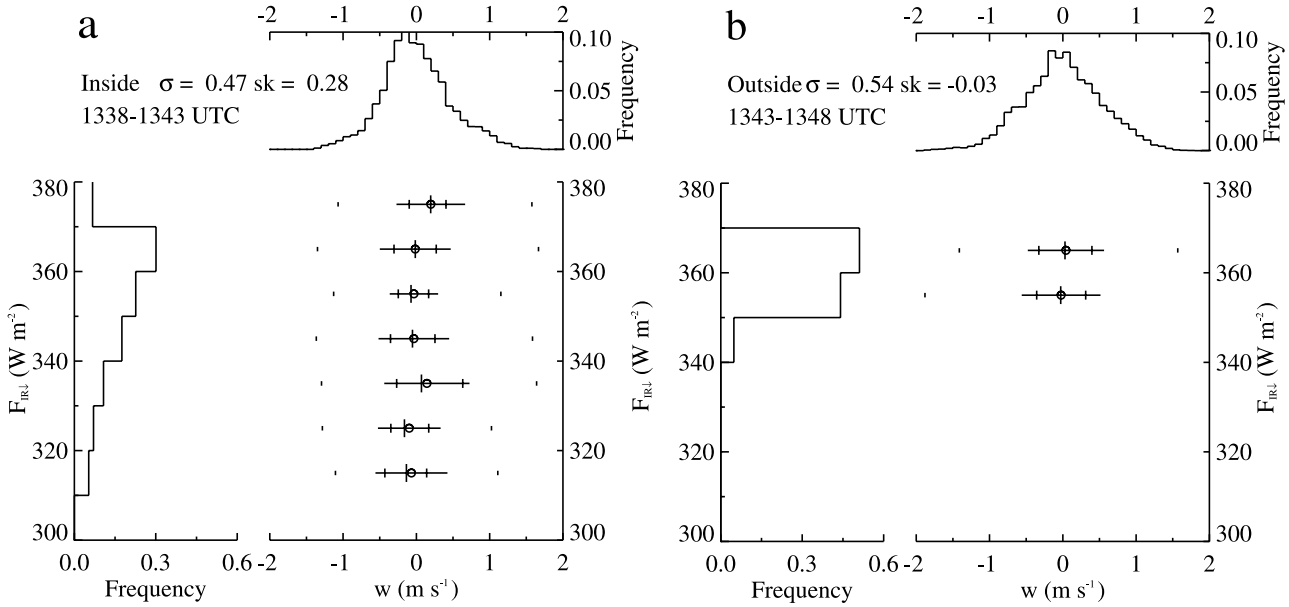

Figure 11. Vertical velocity statistics sampled (a) inside and (b) outside the pocket. Time segments are chosen as in Figure 10. Shown are the marginal w distributions (top plots) and marginal $F_{IR\downarrow}$ distributions (bottom left plots). Also shown are conditional w distributions sampled within $\Delta F_{IR\downarrow} = 10$ W m^{-2} intervals (bottom right plots). Vertical lines show the minimum, lower quartile, median, upper quartile, and maximum w, respectively. Circles correspond to the mean, horizontal lines correspond to the mean ± one standard deviation, and σ and sk denote the standard deviation and the skewness of the marginal w distributions.

but the possibility that it is composed of other compounds, equally or slightly less hygroscopic than the assumed NH_4HSO_4, cannot be dismissed.

4.1. Origin

[29] Here we explore the origin of the Aitken particles analyzing the spatial context in which they were observed. The presence of Aitken particles in the FT is not indicated in size spectra acquired during the above-cloud circles. During the sounding at the end of the below-cloud #3 circle (Figure 1), CN-to-AMC ratios dropped from 20 ± 6 inside the MBL to 6 ± 2 in the FT. This establishes the point that FT-to-MBL entrainment is an insufficient explanation for the Aitken mode particles observed in the boundary layer. Furthermore, Aitken particles were not detected toward the North American continent (cf. Figure 5, bottom left plots) and prevailing winds were northwesterly both in the FT and MBL, so we assert that the source of the Aitken particles is toward the northwest, most probably because of a particle nucleation event which occurred within the MBL.

[30] Observed nanoparticle growth rates subsequent to particle nucleation events range between 0.003 and 0.01 μm h^{-1} [*Hoppel et al.*, 1994; *Weber et al.*, 1998b; *Jennings and O'Dowd*, 2000]. On the basis of these growth rates ~2 to 4 hours of sustained growth suffices to yield the observed Aitken mode diameter (0.02 μm). However, the elusiveness of the actual nucleation event, and of the source strength of the condensing species, makes affirmative assertions about the age of the Aitken particles difficult.

[31] Conditions inside the pocket, and perhaps also conditions leading to the genesis of pockets of open cells, are favorable for particle nucleation. Broken cloud cover is expected to have enhanced the actinic flux during the daytime, driving the photochemical oxidation of DMS. Inside the pocket, but outside the regions of drizzle, the PCASP was used to estimate the particle surface area. Values of 5.9 ± 0.4 μm^2 cm^{-3} were below the critical threshold of 10 μm^2 cm^{-3} where particle nucleation is favored over condensation [*Clarke et al.*, 1998a]. Similar to our observation, aerosol originating from a nucleation event occurring close to the top of a morning stratocumulus layer were documented by *Hegg et al.* [1991]. These authors found a large increase in CN concentration and these particles did not activate inside a CCN chamber at $s = 1\%$. In their case, however, sampling artifacts or transport across the FT/MBL interface cannot be dismissed [*Paluch and Lenschow*, 1992].

5. Discussion

[32] We document mesoscale contrasts between a pocket of open cells (the pocket) and an adjacent region of stratiform cloud. Inside the pocket narrow cell walls (1–6 km in width), with heavy drizzle, surround cell cores (6–12 km in width) characterized by cloud thinning and even clearing. We document the variable radar echo top heights (Figure 12) and the unusually low accumulation mode concentrations (Figure 9) inside the pocket. Also of note is the fact that the Aitken mode particles are not effective cloud droplet nuclei (section 4) which establishes our initial premise (section 2.4) that droplet nuclei concentrations are approximated by PCASP-measured concentrations. We now propose explanations contributing to the maintenance of pockets of open cells in terms of dynamical and the microphysical mechanisms.

[33] From a dynamical perspective, a transition from stratocumulus-like to cumulus-like circulation can occur in

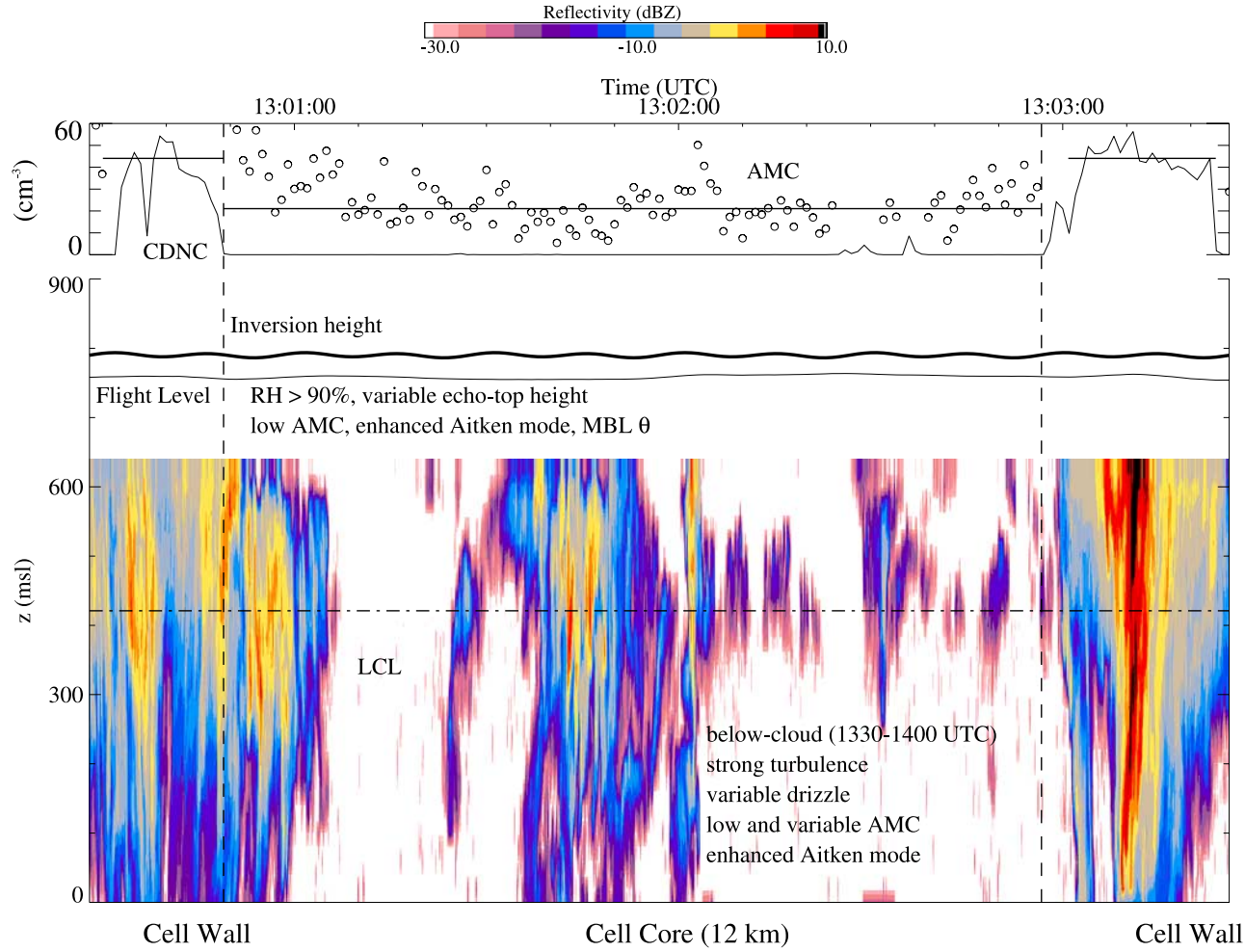

Figure 12. (top) Accumulation mode concentration (AMC) and cloud droplet number concentration time series and (bottom) radar reflectivity profiles (dBZ) acquired during the in-cloud #5 circle between 1300:28–1303:28 UTC. (bottom) C-130 flight level, the estimated top of the inversion, the LCL, cell walls and cell core (Figure 12, bottom), accumulation mode aerosol concentration in the cell core, and cloud droplet number concentration in the cell wall (Figure 12, top).

response to the diabatic effects of precipitation on the MBL [*Stevens et al.*, 1998]. Such large eddy simulation studies demonstrate that within a nocturnal precipitating MBL, cumulus-like updrafts are accompanied by broader and gentler regions of downdraft. This turbulence field is in contrast to smaller-scale eddies, with aspect ratio of order one, typically associated with stratocumulus. Although some aspects of the observations of pockets of open cells are consistent with the simulation, e.g., the cloud spacing within the pocket (Figure 8) and the tendency toward reduced w variance and positive w skewness (Figure 11), the data show the same dominant eddy mode at $f \sim 0.2$ Hz inside the pocket and the surrounding more stratiform region and do not reveal the upscale organization anticipated by the model (Figure 10). The power spectral analysis, however, does not make a convincing case for the absence of cumulus-like circulation within the pocket, and in fact the cell cores may be a manifestation of the model-anticipated downdraft structure. Further, there is some evidence for the presence of gravity waves (section 3.3.1), and if that is indeed the case these may have an organizing influence on the cell wall and cell core structure of the pocket.

[34] From an aerosol and cloud microphysical perspective, pockets of open cells may be viewed as a region of reduced droplet nuclei abundance where the rapid onset of drizzle, combined with spatial variability in droplet nuclei induced by drizzle scavenging, precludes the formation of a stratiform cloud layer. Parcel models which include collision/coalescence demonstrate that in a low droplet nuclei regime cloud top heights are modulated by droplet nuclei abundance [*Hegg*, 1999]. When droplet nuclei abundance is decreased, autoconversion rates are enhanced and mean droplet diameters approach the autoconversion threshold ($D \sim 20$ μm) within a few tens of meters of cloud base [*Pawlowska and Brenguier*, 2003]. In this context autoconversion refers to the self collection of droplets forming precipitation embryos. It follows that the overall effect of reduced droplet nuclei abundance is the accelerated onset of drizzle formation. As droplet mass is shunted into drizzle via autoconversion, updrafts loose condensate during ascent and cloud tops

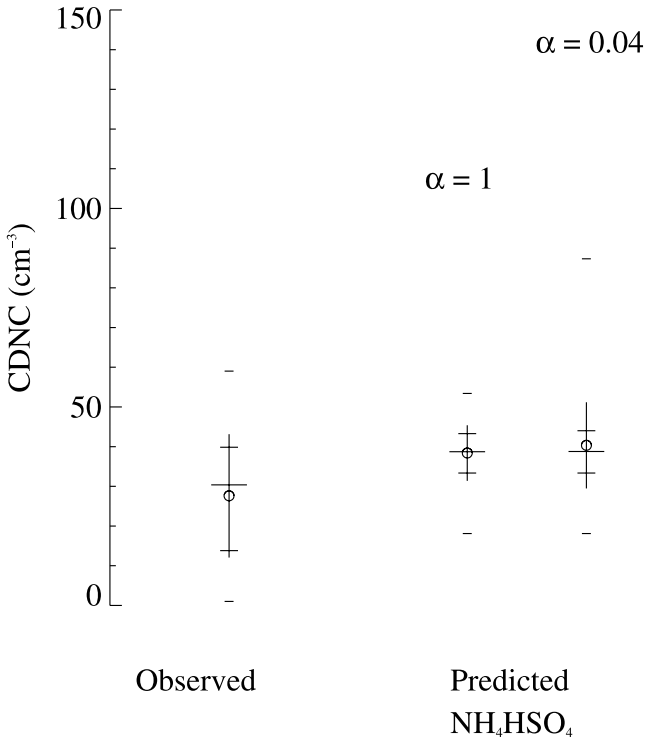

Figure 13. Statistics of observed and predicted ensembles of cloud droplet number concentration inside the pocket. Horizontal lines show the minimum, lower quartile, median, upper quartile, and maximum droplet concentration, respectively. Circles correspond to the mean, and vertical lines correspond to the mean ± one standard deviation of the distribution.

become sensitive to initial droplet nuclei abundance [*Hegg*, 1999]. Observations of low droplet nuclei concentrations (Figure 9) and variable radar echo tops (Figure 12) are consistent with these parcel model predictions.

[35] Both the dynamical and the microphysical mechanisms are causally linked to droplet nuclei abundance. Known sources of droplet nuclei in the remote MBL are entrainment and the sea-to-atmosphere flux. For the former, entrainment velocities ~0.6 cm s^{-1} [*Faloona et al.*, 2005] combined with observed FT-to-MBL aerosol gradients produce a flux which is too weak to compete with removal within the precipitating cell walls where drizzle fluxes are ~10 mm d^{-1}. Observed horizontal winds within the pocket are relatively low (5–8 m s^{-1}) indicating that the sea-to-atmosphere flux is also uncompetitive [*Mason*, 2001; *Nilsson et al.*, 2001]. As a result, the MBL droplet nuclei and particle surface area tendencies are conjectured to be negative, cloud fraction is diminished in response to enhanced rates of autoconversion, aerosol precursor photolysis rates within the MBL are increased, and the region becomes predisposed for particle nucleation. Implicit in this view is the plausibility that cloud processing of the aerosol (i.e., nucleation scavenging, coalescence, and precipitation) perturb the abundance of droplet nuclei within the MBL and thus play a role in regulating cloud fraction and particle nucleation over the oceans.

[36] Because of the implications raised in the foregoing discussion, a word of caution is in order. What we have designated mechanisms are in fact rationalizations of stratocumulus response to low droplet nuclei abundance. Thus these mechanisms are the quintessence of computational models, but the latter are not a priori applicable to pockets of open cells. Consistency between observations and the proposed mechanisms neither fully validates these models nor fully elucidates pockets of open cells. Although we are confident that scarcity of cloud condensation nuclei maintain the pockets, the mechanism itself is not clear. Further insights into the mechanics of this phenomenon will require characterizations of the horizontal fields (i.e., cloud, aerosol, actinic flux, and gaseous precursors), of the thermodynamic stratification, and of the temporal evolution of the internal structure of pockets of open cells.

6. Conclusions

[37] Mesoscale differences between pockets of open cells and surrounding stratiform clouds are reported. In situ data demonstrate that inside pockets of open cells, radar echo tops are variable, droplet nuclei concentrations are low, and Aitken particles dominate aerosol concentration. The latter are suggested to result from a particle nucleation event that occurred within the MBL. It is proposed that low droplet nuclei concentrations maintain pockets of open cells via dynamical and microphysical mechanisms. These linkages between droplet nuclei abundance and pockets of open cells imply that the remote MBL may be more susceptible to modification by cloud condensation nuclei than thought previously.

Appendix A: Instrumentation

A1. Aerosol Size Spectra

[38] The passive cavity aerosol spectrometer probe (PCASP) used during DYCOMS-II is an updated version of this instrument with twice the size resolution of its predecessor. Because there is noise present in the lowest channel of the PCASP, we only utilize PCASP measurements corresponding to sizes larger than 0.1 μm [*Twohy et al.*, 2005]. The manufacturer-defined sizing, which assumes a refractive index of 1.59, was used for our data analysis.

[39] The radial differential mobility analyzer (RDMA) is designed for measurement of aerosol size spectra in the 0.01 to 0.13 μm size range [*Russell et al.*, 1996]. Polydisperse aerosols are brought to charge equilibrium and classified as a function of aerosol electric mobility by varying the electric potential inside the RDMA from 0 to −5000 V and from −5000 to 0 V. We refer to these variations of the RDMA voltage (60 s each) as the upscan and downscan, respectively. Particles classified on the basis of their electric mobility are counted by a condensation particle counter (CPC) where particles larger than 0.008 μm are detected with ~100% efficiency [*Russell et al.*, 1996]. The resulting electric mobility spectra were inverted to size spectra and sizes were calculated from electric mobility using scan-averaged pressure (p) and temperature (T). Particle sizes were interpolated onto a geometrically stepped grid ranging from 0.006 to 0.13 μm with $\Delta \log_{10} D = 0.05$. No attempt was made to correct the size spectra for diffusional broadening.

[40] We construct aerosol size spectra by combining PCASP size spectra measured at sizes larger than 0.13 μm

with RDMA spectra measured at smaller sizes. During flight 2, when abundant Aitken mode particles were present, CN concentrations derived from PCASP/RDMA size spectra were ~35% lower than those from the TSI 3760. Since comparisons made on other flight days agreed within ±10% [*Petters*, 2004], we conjecture that the 35% discrepancy for flight 2 is due to reduced transmission of Aitken mode particles in the tubing leading to the RDMA, compared to transmission in the tubing leading to the TSI 3760. We accounted for the 35% disparity by scaling the fitted concentration of the Aitken mode (i.e., n_1, section 4) until agreement was achieved between total particle concentration, used for the parcel model initialization, compared with averages derived from CN measurements made with the TSI 3760. This correction, however, had an insignificant impact on the concentration of activated cloud droplets predicted in section 4.

A2. Power Spectral Densities

[41] Power spectral densities ($S_w(f) = d\sigma^2/d\log_{10}f$), defined as the w variance per decimal logarithmic frequency interval, were calculated from the 25 Hz time series after removing linear trends and applying a 10% cosine-taper function. These are presented in an area-preserving format by plotting linear values of $S_w(f)$ versus the decimal logarithm of frequency.

A3. Liquid Water Shattering

[42] Aerosol data concurrent with the observation of cloud or drizzle are suspect because of liquid water shattering [*Weber et al.*, 1998a; *Guibert et al.*, 2003]. The method used to select against data segments affected by shattering are described by *Petters* [2004]. In brief, we define a "liquid water reject" event as LWC > 0.1 g m^{-3} or 2D-C > L^{-1} or cloud droplet number concentration >1 cm^{-3} for 1 s, and if this is true we omit aerosol measurements from averages or from plotted time series. There is an instrument-dependent lag between liquid water reject events and the artifact [*Petters*, 2004] and this is accounted for here. Aerosol size spectra were rejected when 3 or more liquid water reject events occurred during the 60 s up or down scans.

A4. Velocities

[43] Updraft velocity was obtained from a gust probe system mounted on the aircraft radome. A bias of up to 0.3 m s^{-1} is reported for this instrument [*Brown*, 1993]. We remove this bias by forcing the mean of w to zero for constant altitude segments.

A5. Remote Sensing

[44] Wyoming Cloud Radar reflectivity data were thresholded five standard deviations above the mean noise level [see *Vali et al.*, 1998] and interpolated onto a 25 Hz × 20 m time-altitude grid (Figure 8) after omitting the first three range gates.

[45] Visible reflectance and brightness temperature at 11 μm wavelength (T_{b11}) data were obtained from channels 1 and 5 of the geostationary operational environmental satellite (GOES 10), respectively. Maximum spatial resolution of these fields is 1x1 km (channel 1) and 4 × 4 km (channel 5). When available, high-resolution T_{b11} data were obtained from channel 5 of the NOAA 12 polar orbiting advanced very high resolution radiometer (AVHRR) at 1 × 1 km maximum spatial resolution.

Notation

D	particle diameter.
$F_{IR\downarrow}$	downwelling IR irradiance.
$T_{\uparrow}$	upwelling IR radiance expressed as radiative temperature.
T_{b11}	satellite derived radiative temperature.
p	pressure.
r	mixing ratio.
r_e	cloud droplet effective radius.
T	temperature.
w	vertical velocity.
α	condensation coefficient.
σ	standard deviation.
sk	skewness.
Φ	azimuth angle.
θ	potential temperature.
$S_w(f)$	power spectral density.
s	supersaturation.
f	frequency.
RH	relative humidity.
AMC	Accumulation Mode Concentration.
AVHRR	Advanced Very High Resolution Radiometer.
CCN	Cloud Condensation Nuclei.
CDNC	Cloud Droplet Number Concentration.
CN	Condensation Nuclei.
CPC	Condensation Particle Counter.
DYCOMS	Dynamics and Chemistry of Marine Stratocumulus.
FT	Free Troposphere.
GOES	Geostationary Operational Environmental Satellite.
IR	Infrared.
LCL	Lifted Condensation Level.
LWC	Liquid Water Content.
LWP	Liquid Water Path.
MBL	Marine Boundary Layer.
NCAR	National Center for Atmospheric Research.
RDMA	Radial Differential Mobility Analyzer.

[46] **Acknowledgments.** This work was funded by NSF ATM-0103951. L. M. Russell acknowledges support from the NSF grant 0104707 and the James S. McDonnell Foundation. We thank numerous employees of NCAR-ATD and the University of Wyoming for their assistance. We also thank Margreet van Zanten for reviewing an early draft of the manuscript. Finally, we thank the editor and the reviewers for their critiques.

References

Ackerman, A. S., O. B. Toon, and P. V. Hobbs (1993), Dissipation of marine stratiform clouds and collapse of the marine boundary layer due to the depletion of cloud condensation nuclei by clouds, *Science*, *262*, 226–229.

Albrecht, B. A. (1989), Aerosols, cloud microphysics, and fractional cloudiness, *Science*, *245*, 1227–1230.

Albrecht, B. A., D. A. Randall, and S. Nicholls (1988), Observations of marine stratocumulus clouds during FIRE, *Bull. Am. Meteorol. Soc.*, *69*, 618–626.

Blanchard, D. C., and A. H. Woodcock (1980), The production concentration and vertical distribution of the sea salt aerosol, *Ann. N.Y. Acad. Sci.*, *338*, 330–347.

Brown, E. N. (1993), Measurement uncertainties of the NCAR air motion system, *NCAR Tech. Note, TN-386+STR*, Res. Aviation Facil., Atmos. Technol. Div., Natl. Cent. for Atmos. Res., Boulder, Colo. (Available as NTIS PB93-184208 from orders@ntis.fedworld.gov)

Cantrell, W., G. R. Cass, Z. Chowdhury, L. S. Hughes, K. A. Prather, S. A. Guazzotti, and K. R. Coffee (2001), Closure between aerosol particles and cloud condensation nuclei at Kaashidhoo climate observatory, *J. Geophys. Res.*, *106*, 28,711–28,718.

Charlson, R. J., J. E. Lovelock, M. O. Andreae, and S. G. Warren (1987), Oceanic phytoplankton, atmospheric sulphur, cloud albedo and climate, *Nature*, *326*, 655–661.

Chuang, P. Y., D. R. Collins, H. Pawlowska, J. R. Snider, H. H. Jonsson, J.-L. Brenguier, R. C. Flagan, and J. H. Seinfeld (2000), CCN measurements during ACE-2 and their relationship to cloud microphysical properties, *Tellus, Ser. B*, *52*, 843–867.

Clarke, A. D., J. L. Varner, F. Eisele, R. L. Mauldin, D. Tanner, and M. Litchy (1998a), Particle production in the remote marine atmosphere: Cloud outflow and subsidence during ACE 1, *J. Geophys. Res.*, *103*, 16,397–16,409.

Clarke, A. D., et al. (1998b), Particle nucleation in the tropical boundary layer and its coupling to marine sulfur sources, *Science*, *282*, 89–92.

Covert, D. S., V. N. Kapustin, P. K. Quinn, and T. S. Bates (1992), New particle formation in the marine boundary layer, *J. Geophys. Res.*, *97*, 20,581–20,589.

Covert, D. S., V. N. Kapustin, T. S. Bates, and P. K. Quinn (1996), Physical properties of marine boundary layer aerosol particles of the mid-Pacific in relation to sources and meteorological transport, *J. Geophys. Res.*, *101*, 6919–6930.

Covert, D. S., J. L. Gras, A. Wiedensohler, and F. Stratman (1998), Comparison of directly measured CCN with CCN modeled from the number-size distribution in the marine boundary layer during ACE 1 at Cape Grim, Tasmania, *J. Geophys. Res.*, *103*, 16,597–16,608.

Faloona, I., D. Lenschow, T. Campos, B. Stevens, M. van Zanten, B. Blomquist, D. Thornton, A. Bandy, and H. Gerber (2005), Observations of entrainment in eastern Pacific marine stratocumulus using three conserved scalars, *J. Atmos. Sci.*, *62*, 3268–3285.

Gerber, H., B. Arends, and A. S. Ackerman (1994), New microphysics sensor for aircraft use, *Atmos. Res.*, *31*, 235–252.

Guibert, S., J. R. Snider, and J.-L. Brenguier (2003), Aerosol activation in marine stratocumulus clouds: 1. Measurement validation for a closure study, *J. Geophys. Res.*, *108*(D15), 8628, doi:10.1029/2002JD002678.

Hegg, D. A. (1999), Dependence of marine stratocumulus formation on aerosols, *Geophys. Res. Lett.*, *26*, 1429–1432.

Hegg, D. A., L. F. Radke, and P. V. Hobbs (1991), Measurements of aitken nuclei and cloud condensation nuclei in the marine atmosphere and their relation to the DMS-cloud climate hypothesis, *J. Geophys. Res.*, *96*, 13,727–18,733.

Hoppel, W. A., G. M. Frick, J. W. Fitzgerald, and R. E. Larson (1994), Marine boundary layer measurement of new particle formation and effects nonprecipitating clouds have on aerosol size distribution, *J. Geophys. Res.*, *99*, 14,443–14,459.

Houghton, J. T., Y. Ding, D. J. Griggs, M. Noguer, P. J. van der Linden, and D. Xiaosu (Eds.) (2001), Climate Change 2001: The Scientific Basis—Contribution of Working Group I to the Third Assessment Report of the Intergovernmental Panel on Climate Change, Cambridge Univ. Press, New York.

Jennings, S. G., and C. D. O'Dowd (2000), Continuous measurements of new particle formation and the radiative effects of coastal particle production plumes, *Rep. Ser. Aerosol Sci.*, *48*, 40–47.

Lenschow, D. H., et al. (1988), Dynamics and chemistry of marine stratocumulus (DYCOMS) experiment, *Bull. Am. Meteorol. Soc.*, *69*, 1058–1067.

Mason, B. J. (2001), The role of sea-salt particles as cloud condensation nuclei over the remote oceans, *Q. J. R. Meteorol. Soc.*, *127*, 2023–2032.

Nicholls, S. (1984), The dynamics of stratocumulus: Aircraft observations and comparisons with a mixed layer model, *Q. J. R. Meteorol. Soc.*, *110*, 783–820.

Nilsson, E. D., U. Rannik, E. Swietlicki, C. Leck, P. P. Aalto, J. Zhou, and M. Norman (2001), Turbulent aerosol fluxes over the Arctic Ocean: 2. Wind-driven sources from the sea, *J. Geophys. Res.*, *106*, 32,139–32,154.

O'Dowd, C. D., and M. H. Smith (1993), Physicochemical properties of aerosols over the northeast Atlantic: Evidence for wind speed related submicron sea-salt aerosol production, *J. Geophys. Res.*, *98*, 1137–1149.

O'Dowd, C. D., J. A. Lowe, M. H. Smith, B. Davidon, C. N. Hewitt, and R. M. Harrison (1997), Biogenic sulphur emissions and inferred non-sea-salt sulphate cloud condensation nuclei in and around Antartica, *J. Geophys. Res.*, *102*, 12,839–12,854.

O'Dowd, C. D., et al. (2002), Marine aerosol formation from biogenic iodine emissions, *Nature*, *417*, 632–635.

Paluch, I. R., and D. H. Lenschow (1992), Comment on "Measurements of Aitken nuclei and cloud condensation nuclei in the marine atmosphere and their relation to the DMS-cloud climate hypothesi" by D. A. Hegg et al., *J. Geophys. Res.*, *97*, 7657–7658.

Pawlowska, H., and J.-L. Brenguier (2000), Microphysical properties of stratocumulus clouds during ACE-2, *Tellus*, *109*, 868–887.

Pawlowska, H., and J.-L. Brenguier (2003), An observational study of drizzle formation in stratocumulus clouds for general circulation model (GCM) parameterizations, *J. Geophys. Res.*, *108*(D15), 8630, doi:10.1029/2002JD002679.

Pazmany, A. L., R. E. McIntosh, R. D. Kelly, and G. Vali (1994), An airborne 95 GHz dual-polarized radar for cloud studies, *IEEE Trans. Geosci. Remote Sens.*, *32*, 731–739.

Petters, M. D. (2004), Cloud condensation nuclei: Measurement, prediction and effects on remote marine stratocumulus clouds, Ph.D. thesis, Dep. of Atmos. Sci., Univ. of Wyo., Laramie.

Pirjola, L., C. D. O'Dowd, I. Brooks, and M. Kulmala (2000), Can new particle formation occur in the marine boundary layer?, *J. Geophys. Res.*, *105*, 26,531–26,546.

Pruppacher, H. R., and J. D. Klett (1997), *Atmospheric and Oceanographic Science Library*, vol. 18, *Microphysics of Clouds and Precipitation*, 2nd ed., Springer, New York.

Quinn, P. K., T. S. Bates, J. E. Johnson, D. S. Covert, and R. J. Charlson (1990), Interaction between the sulfur and reduced nitrogen cycles over the central Pacific Ocean, *J. Geophys. Res.*, *95*, 16,405–16,416.

Raes, F. D. R. V., E. Cuevas, P. F. J. V. Velthoven, and J. M. Prospero (1997), Observations of aerosols in the free troposphere and marine boundary layer of the subtropical northeast Atlantic: Discussion of processes determining their size distribution, *J. Geophys. Res.*, *102*, 21,315–21,328.

Russell, L. M., S. H. Zhang, R. C. Flagan, and J. H. Seinfeld (1996), Radially classified aerosol detector for aircraft-based submicron aerosol measurements, *J. Atmos. Oceanic Technol.*, *13*, 598–609.

Russell, L. M., D. H. Lenschow, K. K. Laursen, P. B. Krummel, S. T. Siems, A. R. Bandy, D. C. Thornton, and T. S. Bates (1998), Bidirectional mixing in an ACE 1 marine boundary layer overlain by a second turbulent layer, *J. Geophys. Res.*, *103*, 16,411–16,432.

Snider, J. R., and J.-L. Brenguier (2000), Cloud condensation nuclei and cloud droplet measurements during ACE-2, *Tellus, Ser. B*, *52*, 828–842.

Snider, J. R., S. Guibert, and J.-L. Brenguier (2003), Aerosol activation in marine stratocumulus clouds: 2. Köhler and parcel theory closure studies, *J. Geophys. Res.*, *108*(D15), 8629, doi:10.1029/2002JD002692.

Stephens, G. L. (1978), Radiation profiles in extended water clouds, I: Theory, *J. Atmos. Sci.*, *35*, 2111–2122.

Stevens, B., W. R. Cotton, G. Feingold, and C. Moeng (1998), Large eddy simulations of strongly precipitating, shallow, stratocumulus-topped boundary layers, *J. Atmos. Sci.*, *55*, 3616–3638.

Stevens, B., et al. (2003a), Dynamics and Chemistry of Marine Stratocumulus—DYCOMS-II, *Bull. Am. Meteorol. Soc.*, *84*, 579–593.

Stevens, B., et al. (2003b), Dynamics and Chemistry of Marine Stratocumulus—DYCOMS-II, *Bull. Am. Meteorol. Soc., 84*, electron. suppl.

Stevens, B., G. Vali, K. Comstock, R. Wood, M. C. Zanten, P. H. Austin, C. S. Bretherton, and D. H. Lenschow (2005), Pockets of open cells (POCs) and drizzle in marine stratocumulus, *Bull. Am. Meteorol. Soc.*, *86*, 51–57.

Twohy, C. H. (1991), Airborne condensation nucleus counter user's guide, *NCAR Tech. Note TN-356+EDD*, 21 pp., Natl. Cent. for Atmos. Res., Boulder, Colo.

Twohy, C. H., M. D. Petters, J. R. Snider, B. Stevens, W. Tahnk, M. Wetzel, L. Russell, and F. Burnet (2005), Evaluation of the aerosol indirect effect in marine stratocumulus clouds: Droplet number, size, liquid water path, and albedo, *J. Geophys. Res.*, *110*, D08203, doi:10.1029/2004JD005116.

Vali, G., R. D. Kelly, J. French, H. Haimov, D. Leon, R. E. McIntosh, and A. Pazmany (1998), Finescale structure and microphysics of coastal stratus, *J. Atmos. Sci.*, *55*, 3540–3564.

van Zanten, M. C., and B. Stevens (2005), On the observed structure of heavily precipitating marine stratocumulus, *J. Atmos. Sci.*, *48*, 40–47.

van Zanten, M., B. Stevens, G. Vali, and D. H. Lenschow (2005), Observations of drizzle in nocturnal marine stratocumulus, *J. Atmos. Sci.*, *62*, 88–106.

Weber, R. J., A. D. Clarke, M. Litchy, L. J. G. Kok, R. D. Schillawski, and P. H. McMurry (1998a), Spurious aerosol measurements when sampling from aircraft in the vicinity of clouds, *J. Geophys. Res.*, *103*, 28,337–28,346.

Weber, R. J., P. H. McMurry, L. Mauldin, D. J. Tanner, F. L. Eisele, S. M. Brechtel, F. Kreidenweis, G. L. Kok, R. D. Schillawski, and D. Baumgardner (1998b), A study of new particle formation and growth involving biogenic and trace gas species measured during ACE 1, *J. Geophys. Res.*, *103*, 16,285–16,396.

Yum, S. S., J. G. Hudson, and X. Yonghong (1998), Comparison of cloud microphysics with cloud condensation nuclei spectra over the summertime Southern Ocean, *J. Geophys. Res.*, *103*, 16,625–16,636.

Zhou, J., O. H. Swietlicki, P. P. Aalto, E. D. Hämeri, K. Nilsson, and C. Leck (2001), Hygroscopic properties of aerosol particles over the central Arctic Ocean during summer, *J. Geophys. Res.*, *106*, 32,111–32,123.

I. Faloona, Department of Land, Air and Water Resources, University of California, Davis, CA 95616-8627, USA.

M. D. Petters, Department of Atmospheric Science, Colorado State University, Fort Collins, CO 80523-1371, USA. (petters@atmos.colostate.edu)

L. M. Russell, Scripps Institution of Oceanography, University of California, San Diego, 9500 Gilman Drive, La Jolla, CA 92093-0221, USA.

J. R. Snider and G. Vali, Department of Atmospheric Science, University of Wyoming, 1000 E. University Avenue, Laramie, WY 82071-3038, USA.

B. Stevens, Department of Atmospheric Science, Box 951565, University of California, Los Angeles, CA 90095-1565, USA.